Articles

Structural and Dynamical Properties of a Partially Unfolded Fe_4S_4 Protein: Role of the Cofactor in Protein Folding[†]

Detlef Bentrop,[‡] Ivano Bertini,*[,‡] Rita Iacoviello,[‡] Claudio Luchinat,[§] Yohei Niikura,[‡] Mario Piccioli,[‡]
Chiara Presenti,[‡] and Antonio Rosato[‡]

Department of Chemistry, University of Florence, Via Gino Capponi, 7, 50121 Florence, Italy, and Department of Soil Science and Plant Nutrition, University of Florence, P. le delle Cascine, 28, 50144 Florence, Italy

Received November 6, 1998; Revised Manuscript Received January 27, 1999

ABSTRACT: Heteronuclear multidimensional NMR spectroscopy was used to investigate in detail the structural and dynamical properties of a partially unfolded intermediate of the reduced high-potential iron−sulfur protein (HiPIP) from *Chromatium vinosum* present in 4 M guanidinium chloride solution. After an extensive assignment of ^{15}N and ^{1}H resonances, NOE data, proton longitudinal relaxation times, and $^{3}J_{HNH\alpha}$ coupling constants as well as ^{15}N relaxation parameters (T_1, T_2, $T_{1\rho}$, and $^{1}H-^{15}N$ NOE) were obtained and used to build a structural model of the intermediate. The Fe_4S_4 cluster of the HiPIP plays a decisive role in determining the resulting structure, which is random in the N-terminal half of the protein and partially organized in the loops between the cysteines bound to the cluster. Consistent with the structural data, the backbone mobility is typical of folded proteins in the regions where there are elements of structure and increases with the structural indetermination.

It was reported earlier (*1*) that the reduced high-potential iron−sulfur protein (HiPIP)[1] from *Chromatium vinosum* (*Cv*) undergoes a reversible partial denaturation in the presence of guanidinium chloride (GdmCl) and gives rise to a stable intermediate at a concentration of about 4 M denaturing agent. The equilibrium between the native and the intermediate state is slow on the NMR time scale and both species are observed by NMR spectroscopy (*1*). HiPIPs are small electron-transfer proteins containing a Fe_4S_4 cluster with 3+ or 2+ charge depending on the oxidation state (*2*−*4*). The oxidized HiPIP rapidly decomposes into the unfolded apoprotein and into the inorganic components of the cluster when GdmCl is added to the solution (*1*). It was suggested that the formation of the intermediate species at any extent deshields the oxidized cluster from the solvent and causes its collapse. Since the cluster is rather stable in the reduced species, its role in opposing to the denaturing action of GdmCl can be investigated. However, it has also been shown that the formation of a stable intermediate is rather unique among HiPIPs and also among other Fe−S proteins (*5*).

Whereas the studies of unfolded, partially folded, or partially unfolded proteins are relatively numerous (refs *6*−*8* and references therein; *9, 10*) little is known about the role of a metal cofactor in protein folding/unfolding (*11*−*13*), from both the structural and dynamical point of view. An appropriate approach is the use of multidimensional heteronuclear NMR spectroscopy, which is, however, hampered by the possible existence of partially (un)folded conformers interconverting one into the other. Depending on the time scale of the interconversion, this disordered situation can lower the quality of the NMR spectra and make their interpretation difficult. In the present case, there is also the paramagnetism of the cluster, which contributes to the broadening of resonance lines (*14*).

The intermediate state of the reduced HiPIP from *Cv* in the presence of GdmCl had been studied previously through the solvent exchangeability of backbone amide protons in order to monitor its increased mobility with respect to the native state (*1*). We report here a further characterization of this system aiming at (i) the determination of as many structural constraints as possible, (ii) the construction of a structural model for the totally or partially structured sequential stretches, and (iii) the detection of different degrees of backbone mobility associated with the structural properties. The specific properties of paramagnetic metalloproteins were exploited in order to transform the disadvantages of paramagnetism into meaningful structural constraints. $^{3}J_{HNH\alpha}$ values were determined to check whether the Φ dihedral angles of the protein backbone are typical of a

---

[†] Supported by the European Union, TMR program, Network ERBCHRXCT940626, and Large Scale Facility Grant ERBFMGECT 950033, by "Comitato Biotecnologie e Biologia molecolare" of the CNR, Italy, and by MURST ex 40%, Italy.

* To whom correspondence should be addressed: Tel. ++39 055 2757549; Fax ++39 055 2757555; e-mail bertini@lrm.fi.cnr.it.

[‡] Department of Chemistry.

[§] Department of Soil Science and Plant Nutrition.

[1] Abbreviations: *Cv*, *Chromatium vinosum*; EXSY, exchange spectroscopy; GdmCl, guanidinium chloride; HiPIP, high-potential iron−sulfur protein; HMQC, heteronuclear multiple quantum coherence; HSQC, heteronuclear single quantum coherence; INEPT, insensitive nuclei enhanced by polarization transfer; NOE, nuclear Overhauser effect; NOESY, nuclear Overhauser effect spectroscopy; RMSD, root-mean-square-deviation; TOCSY, total correlation spectroscopy. TPPI, time-proportional phase incrementation.

10.1021/bi982647q CCC: $18.00

random coil or of a partially organized species. Furthermore, ^{15}N T_1, T_2, and $T_{1\rho}$ relaxation times as well as ^{1}H−^{15}N NOEs were measured to characterize the dynamic properties of the intermediate state in terms of its mobility on the time scales that are accessible to modern NMR methods.

MATERIALS AND METHODS

Sample Preparation. Reduced, recombinant *Cv* HiPIP was expressed as a fusion protein in *Escherichia coli* and purified according to previously published protocols (*15*, *16*). Uniformly ^{15}N labeled samples were prepared by growing *E. coli* strain TOPP1 (Stratagene) containing the plasmide pEBCV10 on M9 minimal medium with 0.5 g/L $(^{15}NH_4)_2SO_4$. For each sample approximately 10 mg of purified protein were exchanged into a final volume of 350 μL of 20 mM potassium phosphate (pH 6.7) by ultrafiltration (Centricon-3 tube). All samples were prepared under an argon atmosphere. To obtain the unfolding intermediate of *Cv* HiPIP, a carefully degassed 10 M solution of guanidinium chloride (Sigma) in 20 mM potassium phosphate (pH 6.7) was added to the protein solution under anaerobic conditions. Addition of 220 μL of GdmCl stock solution resulted in a 1:1 mixture of native and partially unfolded protein, whereas an addition of 280 μL of GdmCl stock solution was necessary for a sample with a 1:4 ratio of native and intermediate form. A sample of unlabeled *Cv* HiPIP for a ^{1}H−^{1}H NOESY spectrum in D_2O was prepared in an analogous manner by addition of a solution of deuterated GdmCl to 26 mg of protein dissolved in the above buffer in 99.8% D_2O. GdmCl was deuterated by repeated dissolution in D_2O and evaporation of the solvent under vacuum.

NMR Spectroscopy. All NMR experiments were recorded at 293 K on Bruker Avance 800 and 600 spectrometers.

One-dimensional (1D) ^{1}H NOE difference spectra were recorded after selective irradiation of hyperfine-shifted and fast-relaxing resonances by previously described acquisition schemes (*17*, *18*) at 800 MHz. In the case of ^{15}N-labeled samples, ^{15}N decoupling during acquisition was employed. Typically, a repetition rate of 3.2 s^{-1} and irradiation times of 154 ms were used.

To detect connectivities between amide cross-peaks of the native and the intermediate state, 2D HSQC−EXSY spectra on a sample containing a 1:1 mixture of the two states were collected with mixing times of 10, 30, 60, and 100 ms. Typically, a relaxation delay of 900 ms and a delay of 5.5 ms for the INEPT transfer were used; water suppression was achieved by presaturation during the relaxation delay and the mixing time; spectral windows of 10 000 Hz (^{1}H) × 4054 Hz (^{15}N) were used. Several series of inversion−recovery ^{15}N HSQC experiments ($P180°_H-\tau-$HSQC) were carried out at 800 MHz to measure the nonselective longitudinal relaxation rates of HN protons. The τ delays of the two sets of experiments performed on the native protein were as follows: (i) 2, 3, 5, 13, 21, 31, 51, 81, 121, 201, and 301 ms; (ii) 30, 50, 70, 100, 150, 250, 350, 510, 710, and 1010 ms. For the intermediate state, one set of inversion−recovery HSQC spectra with delays of 12, 16, 20, 24, 30, 40, 50, 60, 80, 100, 120, and 150 ms was recorded. To detect cross-peaks involving fast relaxing protons, the relaxation delay was set to 300 ms and the dephasing delay to 2.6 ms in the two sets of experiments with short τ delays.

To identify spin systems for the sequential assignment of the intermediate state of *Cv* HiPIP, two TOCSY−^{15}N HMQC experiments with spin-lock mixing times of 35 and 60 ms were carried out at 600 MHz. They were recorded with 2048 (^{1}H) × 111 (^{15}N) × 288 (^{1}H) data points and suppression of the solvent signal by the WATERGATE technique (*19*). Other 3D experiments for the determination of structural constraints were performed at 800 MHz. A Watergate NOESY−^{15}N HSQC experiment was carried out with a mixing time of 180 ms. Spectral windows of 7813 Hz (^{1}H) × 2000 Hz (^{15}N) × 7576 Hz (^{1}H) were employed; the number of data points was equal to that of the TOCSY−^{15}N HMQC experiments. A HNHA spectrum (*20*) to extract $^3J_{HNH\alpha}$ coupling constants was collected with 2048 (^{1}H) × 91 (^{15}N) × 96 (^{1}H) data points. States-TPPI was used for quadrature detection in both indirect dimensions.

A ^{1}H−^{1}H NOESY (*21*) experiment on an unlabeled sample of *Cv* HiPIP in the intermediate state was recorded in D_2O solution with a mixing time of 100 ms at 800 MHz. Water suppression was achieved with a WATERGATE sequence (*19*), whereas the residual signal of GdmCl was suppressed by continuous coherent irradiation during the relaxation delay and the mixing time. A total of 4096 × 620 data points were acquired over a spectral window of 9762 Hz in both dimensions.

^{15}N T_1^{-1} relaxation rates were measured by use of a previously reported sequence (*22*), modified to remove cross-correlation effects during the relaxation delay (*23*). ^{15}N T_2^{-1} relaxation rates were measured by a commonly used scheme (*23*, *24*). 2048 × 220 data points were collected with 16 scans for each experiment over 5682 Hz in the ^{1}H dimension and 1937 Hz in the indirect ^{15}N dimension. The recycle delay was 2.2 s. A commercially available algorithm for linear prediction was used for the indirect dimension. Quadrature detection in the *F*1 dimension was obtained by the TPPI (*25*) method. Presaturation was used to suppress the strong solvent signal. Nine experiments were collected to measure the ^{15}N T_1 relaxation times, with recovery delays of 10, 70, 150, 250, 380, 540, 740, 1000, and 1350 ms. Eight experiments were carried out to measure the ^{15}N T_2 values, with delays of 7.6, 15.2, 30.4, 60.8, 106.4, 167.2, 258.4, and 344.4 ms. ^{1}H−^{15}N NOEs were also measured by use of a previously reported sequence (*26*). ^{1}H saturation was kept for 2.5 s and preceded by a 500 ms presaturation pulse. In the reference experiment, ^{1}H saturation was replaced by two 1 ms trim pulses spaced by 1 ms. All ^{15}N relaxation time and NOE measurements were carried out at 600 MHz.

All NMR data were processed with the standard Bruker software (XWINNMR). The program XEASY (ETH Zürich) (*27*) was employed for spectral analysis and assignment.

Calculation of a Structural Model of the Cv HiPIP Unfolding Intermediate. The calculations of a structural model for the unfolding intermediate of *Cv* HiPIP were carried out with the program DYANA (*28*). Various types of conventional and nonconventional "paramagnetic" constraints have been utilized in the present work:

(i) Dipolar Connectivities. The volumes of unambiguously assigned NOESY cross-peaks between protons of amino acid residues in the C-terminal half of the protein (residues 39−85) were converted into proton−proton upper distance limits by the program CALIBA (*29*) using five different classes of NOEs (*30*). In total, 145 dipolar connectivities from

NOESY spectra were used (127 from NOESY−HSQC and 18 from 2D NOESY). Dipolar connectivities of hyperfine shifted cysteinyl βCH_2 protons obtained from 1D NOE difference experiments were transformed into upper distance limits by means of the steady-state approximation (*31*) with a rotational correlation time of 6.4 ns. The latter value was obtained from the calculations in the model-free formalism described below.

(ii) Distance Constraints for the Cluster. The Fe_4S_4 cluster was included in the structure calculations as described previously for the native protein through the addition of an artificial amino acid residue of the type Cys−S_γ−Fe−S to the DYANA residue library (*32*). A total of 26 upper and 26 lower distance limits between pairs of Fe, S, and S_γ atoms, respectively, were imposed to define the cubane cluster geometry. This is the minimum number of constraints necessary to build up the cluster with its geometry known from crystallography and does not impose any restraints on the backbone or C_β atoms of the cysteines involved. Moreover, these constraints leave undefined the chirality of the peptide folding around the iron−sulfur cluster.

(iii) Dihedral Angle Constraints Derived from the Hyperfine Shifts of Cysteinyl βCH_2 Protons. Constraints for the C_α−C_β−S_γ−Fe dihedral angle of cysteines coordinating to a $[Fe_4S_4]^{2+}$ cluster can be determined from the hyperfine chemical shifts of their βCH_2 protons through the following Karplus-type relationship (*33*, *34*):

$$\delta = a \sin^2 \theta + b \cos \theta + c \tag{1}$$

where θ is the dihedral angle between the plane defined by S_γ, C_β, and the observed nucleus (C_α or H_β) and the plane defined by the C_β, S_γ, and Fe atoms. The values of a, b, and c (11.5, −2.9, and 3.7 ppm, respectively) have been previously parametrized for $[Fe_4S_4]^{2+}$ centers in iron−sulfur proteins (*2*, *33*). To select the appropriate value of θ among the possible solutions of eq 1, the reported stereospecific assignment of the cysteinyl βCH_2 protons (*1*) was used.

(iv) Dihedral Angle Constraints Derived from Scalar Coupling Constants. A 3D HNHA experiment (*20*) was performed on both the native *Cv* HiPIP and the intermediate state to measure the $^3J_{HNH\alpha}$ coupling constants. They were corrected according to Vuister and Bax (*20*) in order to account for the different relaxation of antiphase and in-phase coherence. The $^3J_{HNH\alpha}$ coupling constant was increased by 5%, 10%, and 20% if the T_1 relaxation time of the HN proton involved was higher than 130 ms, between 80 and 130 ms, and below 80 ms, respectively. This correction was applied to the ^3J values of both the native and the intermediate state. In this way, also $^3J_{HNH\alpha}$ coupling constants involving residues in the vicinity of the paramagnetic center can provide meaningful structural information (*35*).

(v) Distance Constraints Involving the Metal Ions Derived from Nonselective T_1 Relaxation Times. Inversion−recovery ^1H−^{15}N HSQC experiments were performed to determine the nonselective longitudinal relaxation rates of amide protons (see above). The intensities of each inversion−recovery HSQC cross-peak were plotted as a function of the delay time t and fitted to

$$I(t) = I(\infty) - [I(\infty) - I(0)] \exp(-t/T_1^{\text{eff}}) \tag{2}$$

where $I(0)$, $I(\infty)$, and T_1^{eff} are the three parameters to be optimized. Their values were calculated through a nonlinear least-squares fit. All errors were within ±20% for the series with short delays tailored for the detection of fast-relaxing amide protons (see above) and within ±15% for the set of experiments with delays up to 1010 ms on the native *Cv* HiPIP. Nonselective T_1 relaxation times of backbone HN protons with $T_1^{\text{eff}} < 200$ ms were transformed into DYANA constraints following the procedure outlined in ref *35*. Briefly, the diamagnetic component of the nuclear relaxation rate, ρ^{dia}, must be estimated and subtracted from $(T_1^{\text{eff}})^{-1}$ of the paramagnetically relaxed proton to obtain the paramagnetic component, ρ^{para}. The diamagnetic contribution to nuclear relaxation rates was assumed to be 4 s^{-1} for all protons. Upper distance limits, d, were obtained from the ρ^{para} values by

$$d_i = K(\rho_i^{\text{para}})^{-1/6} \tag{3}$$

K was determined iteratively comparing the calculated metal−proton distances with those in the structure of the native protein. A final value of 9.64 Å $s^{-1/6}$ was used. Lower distance limits for the paramagnetically relaxed HN protons were calculated in an analogous manner with a K value of 5.85 Å $s^{-1/6}$.

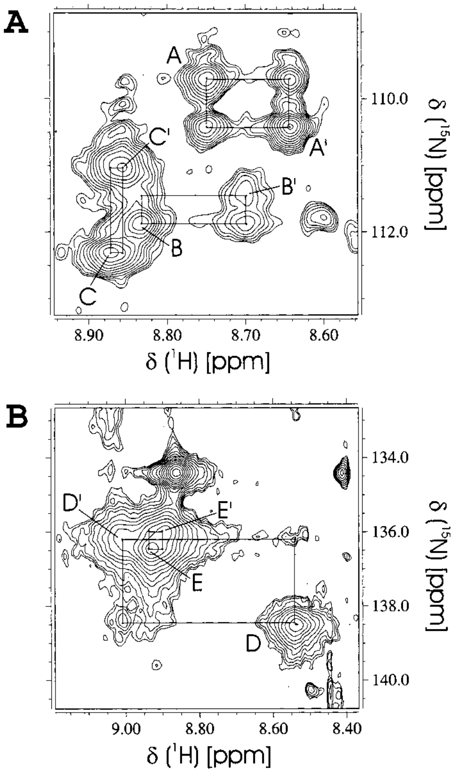

FIGURE 1: (A) HSQC-EXSY spectrum of a 1:1 mixture of native and intermediate *Cv* HiPIP (mixing time 60 ms) showing the exchange correlations between backbone amide cross-peaks of the native and intermediate species. Primed peaks correspond to the intermediate species. Peak A, Gly35; peak B, Gly 55; peak C, Gly 68. (B) Part of a paramagnetic HSQC-EXSY spectrum with 10 ms mixing time. Peak D, Ser 79; peak E, Gln 47.

Analysis of ^{15}N Relaxation Data. ^{15}N R_1, R_2, and $R_{1\rho}$ relaxation rates were determined by fitting the peak volume data, measured as a function of the relaxation delay, to a single exponential using the Levenberg−Marquardt algorithm (*36*, *37*) as described in the literature (*38*). Uncertainties in the fitted rates were evaluated by a Monte Carlo approach similar to the one previously used by several researchers (*38*−*40*). Heteronuclear NOE effects were calculated as the ratio of peak volumes in spectra recorded with and without ^{1}H saturation. The error on the heteronuclear NOE values was estimated by measuring peak volume uncertainties and evaluating the error propagation. The ^{15}N relaxation data were analyzed in terms of the model-free formalism (*41*) through the Modelfree program, version 3.1, following previously described methodology (*38*). Uncertainties on the obtained parameters were estimated by Monte Carlo sampling, as implemented in the program Modelfree.

Off-resonance rotating-frame relaxation rates are given by (*42*−*45*)

$$R_{1\rho}^{\text{off}} = R_1\cos^2\theta_i + R_{1\rho}^{\text{on},\infty}\sin^2\theta_i + K\sin^2\theta_i\,\frac{\tau_{\text{ex}}}{1+\tau_{\text{ex}}^{2}\omega_{\text{eff},i}^{2}} \tag{4}$$

where R_1 is the longitudinal relaxation rate of the ^{15}N nucleus of the *i*th residue; $R_{1\rho}^{\text{on},\infty}$ is the on-resonance rotating frame relaxation rate for an infinitely large effective field amplitude (where all exchange contributions are dispersed to zero); K is a constant equal to $p_{\text{a}}p_{\text{b}}\delta\Omega^2$, where p_{a} and p_{b} are the populations of the two states a and b between which the exchange process occurs and $\delta\Omega$ is the ^{15}N chemical shift difference between the two states; τ_{ex} is the time constant for the exchange process observed for the ^{15}N nucleus of the *i*th residue. θ_i is defined by

$$\theta_i = \arctan\left(\frac{\omega_1}{\Delta\omega_i}\right) \tag{5}$$

$\Delta\omega_i = \omega_{\text{RF}} - \omega_i$, where ω_{RF} is the spin-lock frequency and ω_i is the Larmor frequency of the ^{15}N nucleus of the *i*th residue. ω_1 is the effective spin-lock magnetic field applied. $\omega_{\text{eff},i}$ is equal to $(\Delta\omega_i^2+\omega_1^2)^{1/2}$. Equation 4 can be rearranged as

$$\frac{R_{1\rho}^{\text{off}} - R_1\cos^2\theta_i}{\sin^2\theta_i} = R_{1\rho}^{\text{off,cor}} = R_{1\rho}^{\text{on},\infty} + K\,\frac{\tau_{\text{ex}}}{1+\tau_{\text{ex}}^{2}\omega_{\text{eff},i}^{2}} \tag{6}$$

The experimental $R_{1\rho}^{\text{off,cor}}$ values were fitted as a function of the amplitude of the effective applied spin-lock according to the above equation, where K and τ_{ex} were used as adjustable parameters.

RESULTS

In all NMR experiments, the resonances of the intermediate species in the unfolding process of reduced *Cv* HiPIP could be distinguished from those of the native species. The ratio of the two forms is determined by the concentration of GdmCl in the solution (*1*).

Resonance Assignment of the Intermediate State and Determination of Structural Constraints. Part of a 2D HSQC−EXSY spectrum recorded at 800 MHz on a sample containing about 50% of the intermediate species is shown in Figure 1A. This spectrum provided the assignment of 35 amide cross-peaks of the intermediate state through their connectivities to the corresponding cross-peaks of the native state.

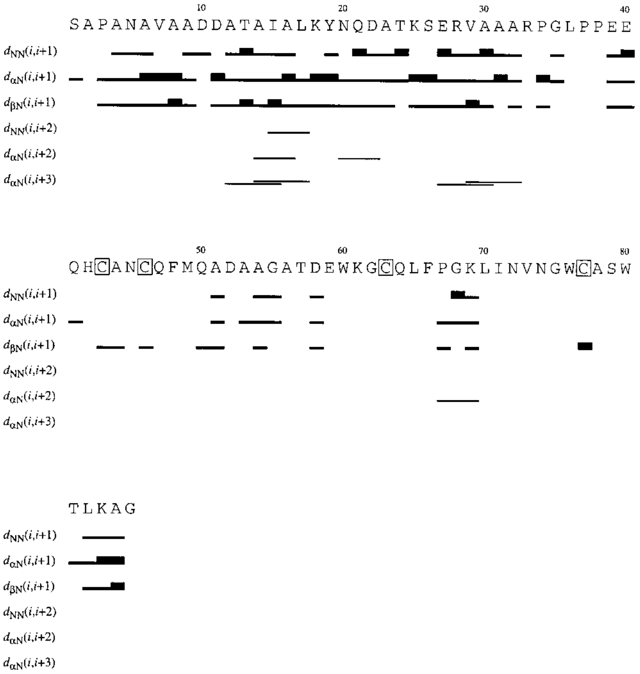

FIGURE 2: Schematic plot of sequential and medium-range NOEs involving HN, Hα, and Hβ protons in the partially unfolded state of *Cv* HiPIP. The cluster ligating cysteines are indicated by squares. The relative NOE intensity is indicated by the width of the bars in the diagram.

Fast hyperfine relaxation rates are expected to hamper the polarization transfer because transverse relaxation can cause the loss of information during the INEPT transfer delay, and obviously the magnetization transfer due to the EXSY part of the experiment can also be affected by the hyperfine relaxation. For this reason, the HSQC−EXSY experiment was repeated with a shorter delay for the INEPT transfer (2.56 ms), relatively short mixing time (10 ms), short relaxation delay (300 ms), and limited number of t_1 increments (256 experiments in *F*1). Under such tailored conditions, seven additional connectivities were observed. Figure 1B shows, as an example of signals that are affected by the paramagnetic center, the peaks involving Ser 79.

Another 26 amide groups that could not be assigned from the 2D experiments due to signal overlap were assigned from the analysis of a 3D NOESY−HSQC spectrum. These assignments of the backbone ^{15}N and HN resonances constituted the basis for the complete analysis of the NOESY−HSQC and TOCSY−HMQC spectra on a sample containing about 80% of the intermediate species. The sequence-specific assignment of the latter species was achieved in a straightforward manner for the N-terminal half of the protein (residues 2−42). Despite the limited ^{1}H chemical shift dispersion that is expected in the case of a largely disordered system, an almost complete assignment of the nonproline amino acid residues in the sequential stretch 2−42 was obtained (77% of all theoretically expected proton resonances and 100% of the nitrogen resonances). The analysis of the ^{15}N-edited 3D NOESY−HSQC spectrum provided a total of 387 NOEs, mostly arising from sequential and intraresidual connectivities (Figure 2).

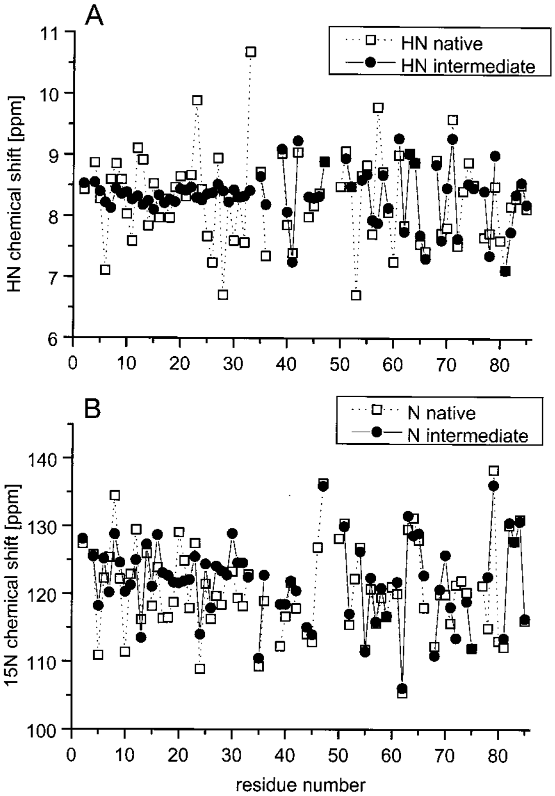

FIGURE 3: (A) Backbone amide proton chemical shifts of *Cv* HiPIP in the native (□) and the intermediate (partially unfolded) state (●) versus the residue number. (B) Backbone amide nitrogen chemical shifts of *Cv* HiPIP in the native (□) and the intermediate (partially unfolded) state (●) versus the residue number.

For the native *Cv* HiPIP an assignment of the amide resonances is available for 75 out of the 79 non-proline residues from Ala 2 to Gly 85. In the intermediate state 68 amide peaks out of 79 have been assigned. The unassigned resonances are the same as those in the native state (Cys 43, Phe 48, Met 49, and Trp 76). In addition, no amide peaks were observed for Cys 46, Gln 50, Ala 53, Trp 60, Val 73, Cys 77, and Trp 80. The resulting assignment of the intermediate state is reported as Supporting Information and a summary of the observed sequential and medium-range NOEs is schematically depicted in Figure 2.

A comparison of the ^1H and ^{15}N chemical shifts of backbone resonances in the native and intermediate state is presented in Figure 3. The distribution of chemical shift differences is clearly not homogeneous over the entire sequence but rather reflects a significant structural change in the first half of the sequence and an overall more conservative behavior in the C-terminal half. In the latter, only small differences between the native and the intermediate state are observed for most of the residues, indicating a nativelike conformation. When the backbone chemical shifts of the *Cv* HiPIP unfolding intermediate are compared to those measured in random coil peptides (*46*), it is clear from the small differences observed in the N-terminal half that this part of the protein adopts a random coil conformation in the intermediate state.

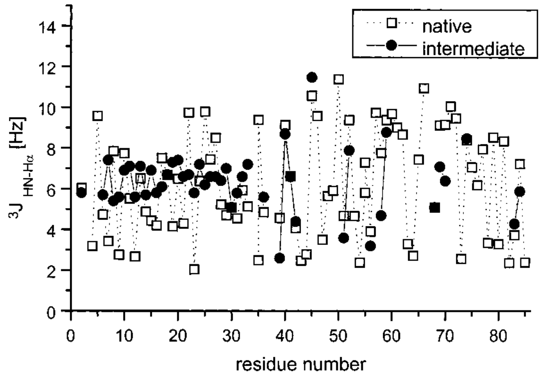

FIGURE 4: $^3J_{HNH\alpha}$ coupling constants of *Cv* HiPIP in the native (□) and the intermediate (partially unfolded) state (●) versus the residue number. For those residues of the native HiPIP for which an experimental $^3J_{HNH\alpha}$ value from the HNHA spectrum was not available (residues 10, 14, 28, 43, 44, 46−49, 58, 62, 64−65, 68, 76−81, and 85), the coupling constant was backcalculated from the corresponding Φ angle in the crystal structure of *Cv* HiPIP [PDB entry 1hip (*62*)] using the Karplus equation with the parameters in ref *20*.

More information on the structural properties of the intermediate state was extracted from a HNHA spectrum (*20*), which was compared to the analogous spectrum recorded on the native *Cv* HiPIP in order to obtain $^3J_{HNH\alpha}$ coupling constants in both states. Despite the limitations arising from the relatively small dispersion in chemical shifts, accurate ^3J values could be obtained for 46 residues of *Cv* HiPIP in the intermediate state. For the native protein 58 $^3J_{HNH\alpha}$ coupling constants were determined. Figure 4 depicts a plot of the $^3J_{HNH\alpha}$ values in the intermediate and native state versus the residue number. For the intermediate state, a comparison with random coil $^3J_{HNH\alpha}$ values (*47*) shows small differences (in the ±1 Hz range) for the sequential stretch 2−38, whereas much larger differences are observed in the C-terminal part of the protein. These results agree with the above chemical shift analysis.

To derive dihedral angle restraints for the DYANA calculations, the classification of $^3J_{HNH\alpha}$ coupling constants described in ref *35* was used. Four coupling constants were bigger than 8 Hz and the corresponding Φ angles were constrained between −155° and −85° (for residues 40, 45, 59, and 74). For five amino acid residues with $^3J_{HNH\alpha} < 4.5$ Hz (residues 39, 42, 51, 56, and 83), the Φ angle was assumed to be in the −80° to −20° range. In the case of Asp 52 with a $^3J_{HNH\alpha}$ of 7.9 Hz (9.4 Hz in the native protein), a Φ angle between −170° and −70° was imposed. Thus, a total of 10 backbone dihedral angle constraints were used for the calculations of a structural model of the partially unfolded protein.

The previously reported stereospecific assignment of the βCH_2 protons of the cluster coordinating cysteines (*1*) was used to derive χ_2 dihedral angle restraints (*33*, *48*−*50*) for these residues. In the present case, three χ_2 constraints could be obtained for cysteines 43, 63, and 77 (Table 1). For these cysteines the actual χ_2 values in the native protein are within the limits of the experimental restraints of the intermediate state, thus indicating that not only the cluster topology but also the dihedral angles of the coordinating side chains are retained. For Cys 46, a discrimination among the possible χ_2 values was not feasible.

The contact shift experienced by cluster-coordinating cysteines can be exploited to perform 1D NOE difference experiments on their well-isolated hyperfine-shifted proton resonances. Upon selective irradiation of the four hyperfine-

Table 1: χ_2 Angle Constraints for the Cluster Coordinating Cysteines in the Intermediate State of Reduced *Cv* HiPIP

residue	χ_2 angle constraint	χ_2 angle in the native protein[a]
Cys 43	[−100, −20]	−75
Cys 46		−163
Cys 63	[53, 142]	128
Cys 77	[−124, −44]	−90

[a] $\mathrm{Fe{-}S_\gamma{-}C_\beta{-}C_\alpha}$ dihedral angles measured in the crystal structure of *Cv* HiPIP [PDB entry 1hip (*62*)].

Table 2: One-Dimensional NOE-Derived Upper Distance Limits in the DYANA Calculations of a Structural Model of the *Cv* HiPIP Unfolding Intermediate

cysteine residue	βCH$_2$ proton	NOE connectivity	upper distance limit (Å)
43 Cys	Hβ3	43 Cys Hα	4.4
	Hβ3	44 Ala HN	4.0
	Hβ3	44 Ala MB	4.7
	Hβ3	49 Met Hγ2	4.4
	Hβ3	49 Met Hγ3	5.1
	Hβ3	49 Met ME	3.9
	Hβ3	71 Ile MD	4.0
	Hβ3	73 Val Hα	3.6
	Hβ3	73 Val Hβ	4.7
	Hβ3	73 Val MG1	4.5
	Hβ3	73 Val MG2	4.5
46 Cys	Hβ3	44 Ala HN	4.7
	Hβ3	46 Cys HN	3.2
	Hβ3	46 Cys Hα	4.5
	Hβ3	47 Gln HN	4.7
63 Cys	Hβ3	62 Gly QA	4.7
	Hβ3	63 Cys HN	3.4
	Hβ3	63 Cys Hα	3.7
	Hβ3	65 Leu HN	4.7
	Hβ3	66 Phe HN	4.6
	Hβ3	66 Phe QB	4.3
	Hβ3	66 Phe Hα	4.7
77 Cys	Hβ2	77 Cys Hα	4.4
	Hβ2	78 Ala HN	3.4
	Hβ2	78 Ala MB	4.3
	Hβ2	79 Ser HN	4.2

Table 3: T_1^{eff} Relaxation Times and Upper and Lower Distance Limits of Paramagnetically Relaxed Backbone Amide Protons in the Unfolding Intermediate of *Cv* HiPIP Used in the DYANA Calculations of a Structural Model

HN of residue	T_1^{eff} (ms)	upper distance limit (Å)	lower distance limit (Å)
Ala 44	43.7	5.90	3.58
Asn 45	55.9	6.21	3.77
Gln 47	28.8	5.45	3.31
Lys 61	165.8	8.56	5.20
Gly 62	123.5	7.62	4.62
Cys 63	37.0	5.71	3.47
Gln 64	45.2	5.94	3.61
Leu 65	10.8	4.60	2.79
Ile 71	48.3	6.00	3.66
Asn 74	164.2	8.52	5.17
Gly 75	40.4	5.81	3.53
Ala 78	28.8	5.45	3.31
Ser 79	19.7	5.07	3.08
Leu 82	198.0	9.56	5.80
Lys 83	134.8	7.85	4.77

shifted signals of the intermediate *Cv* HiPIP species, 29 NOEs were observed. Eighteen of these were easily assigned by comparison with the analogous 1D NOE spectra of the native protein. With the set of NOEs available at this point, a preliminary family of structures was calculated by DYANA. These structures were screened for protons in vicinity to the hyperfine-shifted cysteinyl βCH$_2$ protons; this information, combined with the chemical shifts of the observed 1D NOEs and with already available assignments from the NOESY−HSQC and EXSY spectra, permitted the assignment of the remaining 11 1D NOEs in an iterative manner. A total of 26 upper distance limits for the final DYANA calculations were obtained from the 1D NOE difference spectra. They are listed in Table 2.

Hyperfine relaxation rates of protons can be used as structural constraints to refine a solution structure that was calculated mainly from conventional NOE constraints as shown before in the case of HiPIP I from *Ectothiorhodospira halophila* (*35*). Given the lack of long-range NOEs in the intermediate state of *Cv* HiPIP, constraints derived from relaxation rates are the only long-range restraints available in this partially unfolded system. The longitudinal relaxation rates of backbone amide protons that were obtained from a "paramagnetic" series of inversion−recovery HSQC spectra on the intermediate species are unique measurements of the distance between the HN of a given residue and the paramagnetic metal center. Moreover, they provide information on structural changes with respect to the native state for which the amide proton relaxation rates were determined, too.

The T_1^{eff} values of the *Cv* HiPIP unfolding intermediate and the corresponding upper and lower distance limits from the polymetallic center that were used as constraints for DYANA are reported in Table 3. In addition, 32 lower distance limits of 8.5 Å were introduced into the DYANA calculations for the backbone HN protons with a $T_1 > 200$ ms. For the HN protons of the two residues, Tyr 19 and Asn 20, that have a strong hyperfine contribution to their longitudinal relaxation rates in the native protein but not in the intermediate state, the distance to the closest iron ion of the cluster in the structure of native *Cv* HiPIP was used as a lower distance limit for DYANA (6.9 and 7.5 Å, respectively).

Fifteen out of the 17 residues that show a hyperfine contribution to their relaxation rates in the native state retain this contribution in the intermediate state. All these 15 residues are located in the C-terminal half of the protein that provides the cluster ligands (Table 3). Their relaxation rates in the intermediate form are very similar to the values in the native state, thus indicating essentially unaltered HN−metal distances. The two residues that lose the hyperfine contribution to the relaxation rate of their HN are Tyr 19 and Asn 20 in the N-terminal half of the protein. This result shows that the N-terminal half of the protein loses its tertiary contacts with the C-terminal half in the presence of GdmCl.

Calculation of a Structural Model. Provided that in the 1−38 segment of the *Cv* HiPIP unfolding intermediate the backbone ^{1}HN and ^{15}N chemical shifts as well as the $^3J_{\mathrm{HNH}\alpha}$ values clearly indicate a random coil situation, an attempt to calculate a structural model has been performed for the C-terminal half using the constraints summarized in Table 4. They refer only to the fragment 39−85 and their distribution along the sequence is reported in Figure 5.

The final DYANA family consisted of 30 structures without consistent constraint violations and an average target function of 0.85 ± 0.18 Å^2. The mean RMSD from the

Table 4: Type and Number of Constraints in the DYANA Calculations of a Structural Model of the *Cv* HiPIP Unfolding Intermediate[a]

type of constraint	number of constraints
upper distance limits	
NOESY−HSQC	127
$^1H-^1H$ NOESY	18
1D NOE	26
nonselective paramagnetic T_1	15
cluster	26
total of upper distance limits	212
lower distance limits	
nonselective paramagnetic T_1	15
$T_1 > 200$ ms	34
cluster	26
total of lower distance limits	75
angle constraints	
ϕ angles	10
χ_2 angles	3
total of angle constraints	13
total number of constraints	300

[a] Only constraints for residues 39−85 are listed.

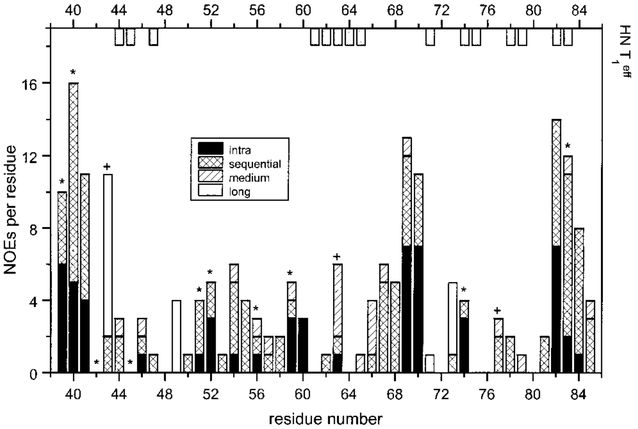

FIGURE 5: Plot of the number of meaningful intraresidual, sequential, medium-range, and long-range NOEs per residue versus the amino acid sequence for the *Cv* HiPIP unfolding intermediate. The asterisk (*) denotes residues for which a ϕ dihedral angle constraint was derived from the $^3J_{HNH\alpha}$ coupling constant. The plus sign (+) identifies the cysteines for which a χ_2 dihedral angle constraint was used in the DYANA calculations. Residues with a short T_1^{eff} for the backbone amide proton that was transformed into upper and lower distance limits for the HN−metal distance are indicated by gray bars on the top axis.

average structure in a best-fit backbone superposition of residues 42−78 is 4.20 ± 1.18 Å for the backbone and 4.98 ± 1.21 Å for all heavy atoms. To analyze the structural data, it is instructive to superimpose the structures on the atoms of the Fe_4S_4 cluster only. In this way, it is possible to compare the loops connecting one cluster-coordinating cysteine to the following one. For such a superposition, the RMSD is higher than that reported above and is plotted as RMSD per residue in Figure 6. The DYANA calculations were repeated without the constraints involving the protein part (i.e., with only the 52 cluster constraints) and the resulting family of 30 structures has a backbone RMSD of 4.96 ± 1.15 Å (for a superposition on the backbone of residues 42−78). The RMSD per residue obtained from a superposition on the cluster atoms only is also shown in Figure 6.

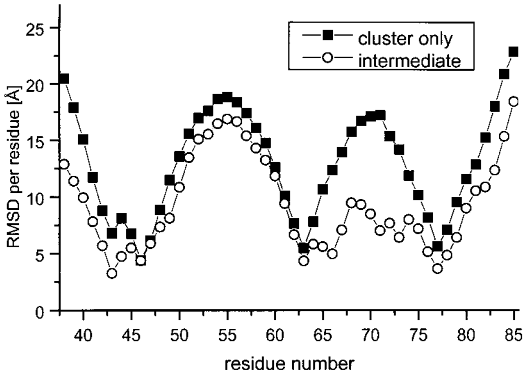

FIGURE 6: Diagram of the pairwise RMSD per residue for the backbone atoms of 15 structures of the DYANA family of the *Cv* HiPIP unfolding intermediate and for 15 structures of a DYANA family calculated with the cluster constraints only. In both cases the structures were superimposed on the eight cluster atoms. The RMSD values are shown for residues 38−85.

Owing to the high RMSD values, a figure displaying the whole family of structures would be useless. Therefore, Figure 7 depicts a stereoview of the two segments of the *Cv* HiPIP intermediate that have a backbone RMSD per residue lower than 10 Å (i.e., the sequential stretches 40−49 and 61−80; the structures were again superimposed on the Fe_4S_4 cluster atoms). For the sake of clarity only nine members of the family are shown. Figure 7 also shows an analogous view of the NMR family of structures of the native HiPIP. It appears that the two folds are similar. It should be noted that the chirality of the polypeptide chain around the cluster in the intermediate state as it results from the DYANA calculations is the same as that observed in the native protein.

Pico- to Nanosecond Mobility. The measured ^{15}N R_1 and R_2 relaxation rates and the $^1H-^{15}N$ NOE values of the *Cv* HiPIP unfolding intermediate are plotted in Figure 8A versus the amino acid sequence. (Tables with the experimental values of R_1, R_2, and heteroNOE are provided as Supporting Information.)

R_1, R_2, and NOE values are given by the following equations (*51*):

$$R_1 = \frac{d^2}{4}[J(\omega_H - \omega_N) + 3J(\omega_N) + 6J(\omega_H + \omega_N)] + c^2 J(\omega_N) \quad (7)$$

$$R_2 = \frac{d^2}{8}[4J(0) + J(\omega_H - \omega_N) + 3J(\omega_N) + 6J(\omega_H) + 6J(\omega_H + \omega_N)] + \frac{c^2}{6}[3J(\omega_N) + 4J(0)] + R_{ex} \quad (8)$$

$$\text{NOE} = 1 + \frac{1}{R_1}\frac{\gamma_H}{\gamma_N}\frac{d^2}{4}[6J(\omega_H + \omega_N) - J(\omega_H - \omega_N)] \quad (9)$$

where

$$c = \frac{\omega_N(\sigma_{\parallel} - \sigma_{\perp})}{\sqrt{3}} \quad (10)$$

$$d = \frac{\mu_0 h}{8\pi^2}\frac{\gamma_H \gamma_N}{{r_{NH}}^3} \quad (11)$$

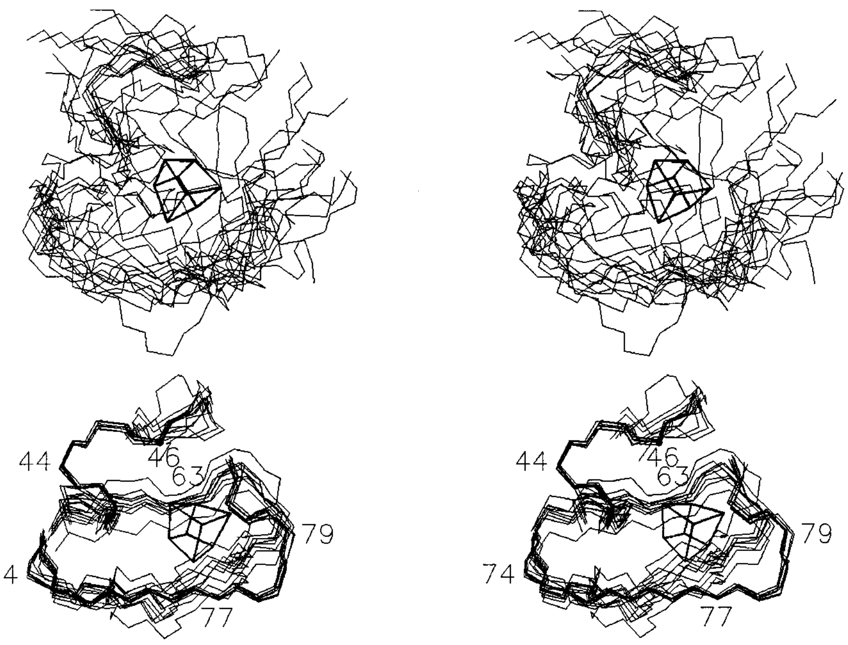

FIGURE 7: (Top) Stereoview of nine members of the DYANA family of the *Cv* HiPIP unfolding intermediate superimposed on the eight cluster atoms. The cluster is indicated by bold black lines. Only the environment of the cluster in which the backbone RMSD per residue is lower than 10 Å is shown. (Bottom) Analogous view of nine structures of the NMR family of native *Cv* HiPIP [PDB entry 1hrr (*32*)]. The figure was prepared with the program MOLMOL (*63*).

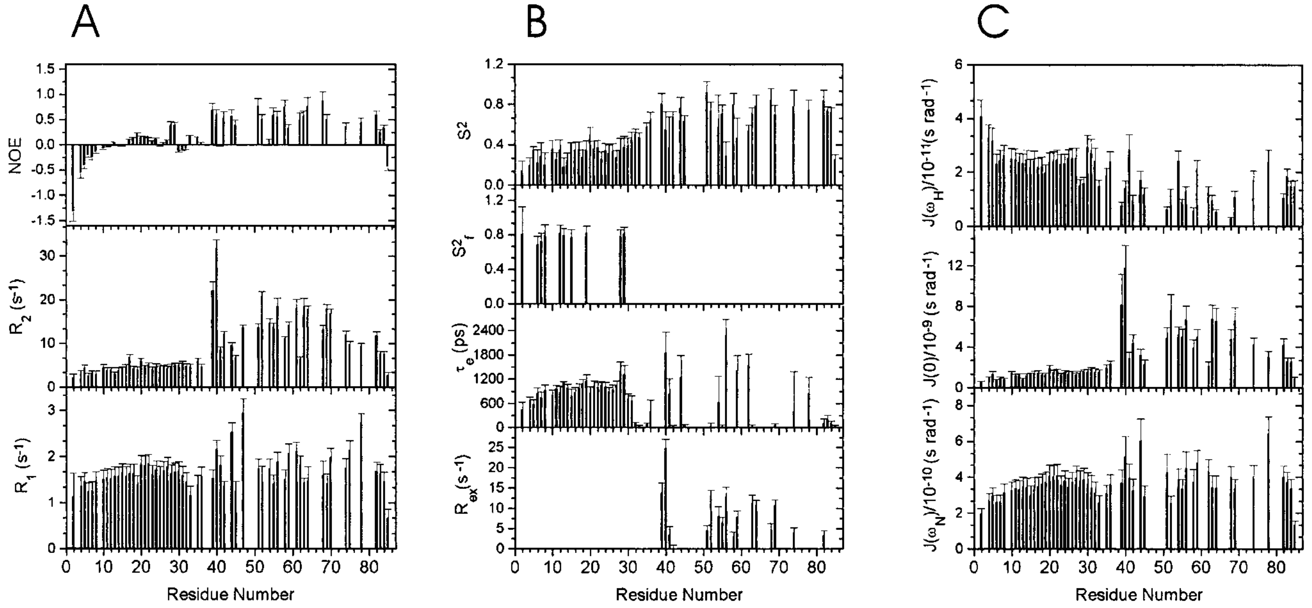

FIGURE 8: Plots of the ^{15}N relaxation parameters and the backbone mobility data versus the residue number. (A) ^{15}N R_1 and R_2 relaxation rates and ^{1}H$-^{15}$N NOE. (B) Parameters of the model-free analysis. (C) Values of spectral density functions $J(\omega_N)$, $J(0)$, and $J(\omega_H)$.

ω_H and ω_N are the Larmor frequencies of the ^{1}H and ^{15}N nuclei, respectively; h is Planck's constant; μ_0 is the permeability of free space; r_{NH} is the N$-$H bond length, taken equal to 1.02 Å; and $\sigma_{\|} - \sigma_{\perp}$ is the difference between the parallel and perpendicular components of the axially symmetric chemical shift tensor (taken equal to -160 ppm). R_{ex} is the exchange contribution to R_2, which may or may not be present.

Each $J(\omega)$ depends on the correlation time for the reorientation of the whole molecule τ_m, on the order parameter S^2, and on the correlation time for the internal motions τ_e according to different models (*52*), which are simplifications of the extended form of the spectral density function proposed by Clore et al. (*53*). The simplest model is

$$J(\omega) = \frac{2}{5}\left[\frac{S^2\tau_m}{1 + (\omega\tau_m)^2}\right] \qquad (12)$$

which contains only S^2 as an adjustable parameter. None of the residues for which reliable ^{15}N relaxation data were obtained could be fitted to this model. All residues in the first half of the molecule (up to residue 38) could be fitted by assuming the following form of the spectral density function:

$$J(\omega) = \frac{2}{5}\left[\frac{S^2\tau_m}{1 + (\omega\tau_m)^2} + \frac{(S_f^{\,2} - S^2)\tau'_e}{1 + (\omega\tau'_e)^2}\right] \tag{13}$$

$$\tau'_e = \frac{\tau_e\tau_m}{(\tau_e + \tau_m)} \tag{14}$$

where S^2 and τ_e are adjustable parameters, whereas S^2_f can be either adjusted or kept equal to 1. In the second half of the molecule, it was necessary to include into the fittings an exchange contribution (R_{ex}) to the transversal ^{15}N relaxation rates (R_2) for the majority of the residues. The form of the spectral density function used for the fitting of the relaxation data of backbone amides belonging to the second half of the molecule was

$$J(\omega) = \frac{2}{5}\left[\frac{S^2\tau_m}{1 + (\omega\tau_m)^2} + \frac{(1 - S^2)\tau'_e}{1 + (\omega\tau'_e)^2}\right] \tag{15}$$

where τ'_e is defined as above. S^2 is an adjustable parameter, together with R_{ex}. τ_e is either adjusted or regarded as negligibly small (i.e., yielding a negligible contribution from the second term in the above spectral density function).

The above models of the spectral density function were discriminated by fitting the ^{15}N relaxation data of each residue with each one of them. The quality of the resulting fittings was then compared, and the most appropriate model was selected on the basis of statistical criteria (*52*).

The results of the model-free analysis are summarized in Figure 8B (a table of the best-fitting values of the different parameters is given in the Supporting Information). The first half of the molecule is characterized by an average S^2 value of 0.33 ± 0.12, whereas this value for the second half is 0.66 ± 0.17.

The experimental relaxation data were also used to map the spectral density function values. This approach to the interpretation of ^{15}N relaxation data, originally proposed by Peng and Wagner (*22*), has the advantage over the model-free approach of not requiring the assumption of isotropic tumbling of the molecule in solution. Thus, it is more suitable for the case of partially denatured proteins (*54*). ^{15}N heteronuclear NOE, R_1, and R_2 data at one magnetic field are not sufficient to derive all the spectral density function values of interest [$J(0)$, $J(\omega_N)$, $J(\omega_H)$, $J(\omega_H - \omega_N)$, and $J(\omega_H + \omega_N)$]. However, as $\omega_H \approx 10\omega_N$, it is possible to reduce the number of the above parameters to three [$J(0)$, $J(\omega_N)$, and $J(\omega_H)$] by neglecting ω_N with respect to ω_H (*39*, *54*, *55*). With the above approximations, the spectral density function values at the frequencies of interest are given by (rearranging eqs 7−9):

$$J_{eff}(0) = \frac{\left[6R_2 - 3R_1 - \frac{18}{5}R_1(\mathrm{NOE} - 1)\frac{\gamma_N}{\gamma_H}\right]}{(3d^2 + 4c^2)} \tag{16}$$

$$J(\omega_N) = \frac{4R_1}{(3d^2 + 4c^2)}\left[1 - \frac{7}{5}(\mathrm{NOE} - 1)\frac{\gamma_N}{\gamma_H}\right] \tag{17}$$

$$J(\omega_H) = 0.2R_1(\mathrm{NOE} - 1)\frac{4}{d^2}\frac{\gamma_N}{\gamma_H} \tag{18}$$

It should be noted that $J_{eff}(0)$ is used instead of $J(0)$ to denote that exchange contributions to R_2 have not been considered explicitly in the present calculations (*56*).

The values of the spectral density functions at $\omega = 0$, ω_N, and ω_H are plotted in Figure 8C versus the residue number, and their values are tabulated in the Supporting Information. The $J(\omega_H)$ values obtained in the first half of the molecule [with an average value of $(2.4 \pm 0.5) \times 10^{-11}$ s rad^{-1}] are sizably larger than in the second half [with an average value of $(1.3 \pm 0.6) \times 10^{-11}$ s rad^{-1}]. The average $J(0)$ value in the first half of the molecule is $(1.3 \pm 0.4) \times 10^{-9}$ s rad^{-1}. In the second half of the protein the obtained values are largely determined by the presence of nonnegligible exchange contributions to R_2 and are consequently much larger than in the first half of the protein (*54*). $J(\omega_N)$ does not give further information; in fact it is determined by contributions that are already included in the other spectral density functions.

Microsecond Mobility. Fourteen residues (39, 51, 52, 54, 55, 56, 59, 61, 63, 64, 68, 69, 74, and 82) showed a distinct dependence of their amide ^{15}N $R_{1\rho}^{\mathrm{off,cor}}$ relaxation rate on the amplitude of the applied spin-lock. As extensively discussed in the literature (*40*, *51*, *57*, *58*), this is due to the presence of local motions on the microsecond time scale. The experimental dependence was fitted as described in the Materials and Methods section with the adjustable parameters K and τ_{ex}. The range of effective spin-lock amplitudes employed in the present work allows the determination of τ_{ex} values in the 10−400 μs range. These values were determined by imposing that the effective amplitude corresponding to the inflection point (where $\omega\tau_{ex} = 1$) is smaller than 4 times the higher amplitude used (which gives the lower limit for τ_{ex}) or larger than a fourth of the lower amplitude used (which gives the upper limit for τ_{ex}). It was found that for a few residues (51, 56, 64, and 82) the fitting required τ_{ex} values higher than those experimentally accessible. Therefore, for these four residues it is only possible to give a lower limit of 400 μs, and no quantitative estimates for the value of K are obtained. The results of the analysis of the $R_{1\rho}$ dependence of the 14 residues indicated above are summarized in Table 5.

DISCUSSION

The body of the experimental NMR data acquired on the present nonnative state of *Cv* HiPIP provides a reasonable picture of the structural and dynamical features of this system and may contribute to the understanding of other systems whose unfolding is not complete due to the presence of structural links that restrict the degrees of freedom of the polypeptide chain. The restriction in this case is provided by the four intact bonds between the Fe_4S_4 cluster and the four cysteine residues and in general can be provided by any coordinated metal ion(s), disulfide bridge(s), cofactor, etc. In this respect, it is instructive to compare the results of the DYANA calculations based on the 300 experimental structural constraints for residues 39−85 with a sample DYANA calculation in which these constraints are omitted. There is only a very modest decrease of the RMSD when the available experimental constraints are included for the

Table 5: Exchange Correlation Times and Exchange Constants for the Residues Exhibiting Chemical Exchange in the Unfolding Intermediate of *Cv* HiPIP

residue	τ_{ex} (μs)	$R_{ex}{}^{a}$ (s $^{-1}$)
Gln 39	48 ± 9	20 ± 4
Ala 51	>400	
Asp 52	30 ± 9	14 ± 5
Ala 54	66 ± 52	31 ± 25
Gly 55	49 ± 10	10 ± 2
Ala 56	>400	
Glu 59	30 ± 23	4 ± 3
Lys 61	74 ± 21	13 ± 4
Cys 63	48 ± 13	15 ± 4
Gln 64	>400	
Gly 68	21 ± 4	7 ± 2
Lys 69	34 ± 9	11 ± 3
Asn 74	81 ± 32	15 ± 7
Leu 82	>400	

[a] $R_{ex} = K\tau_{ex}$ (see eq 4 or 6).

holoprotein. The decrease in degrees of freedom introduced by the mere presence of the cluster is remarkable, and this should be kept in mind for the correct interpretation of the present results.

In the 85-residue HiPIP, the cysteines coordinating the Fe_4S_4 cluster all belong to the second half of the sequence (Cys 43, 46, 63, and 77). The behavior of residues 39−83 is indeed quite different from that of residues 1−38. The $^3J_{HNH\alpha}$ values (Figure 4) show an almost complete conformational averaging of backbone dihedral angles in the first half of the protein; on the other hand, many $^3J_{HNH\alpha}$ values in the second half of the protein do not match the random coil values and are in several cases close to the values in the native protein. The most striking examples are residues 39, 40, 42, 45, 56, 59, 74, and 83. No $^3J_{HNH\alpha}$ values for the cluster-coordinating cysteines are available, but there is independent evidence from the hyperfine shifts of their βCH_2 protons that for three out of four of them the χ_2 dihedral angle (Fe−S_γ−C_β−C_α) is not appreciably different from the value in the native state.

In this light, the information derived from paramagnetic enhancements of the proton longitudinal relaxation rates (Table 3) gains particular significance: of all residues experiencing paramagnetic relaxation enhancements in the native state as a consequence of their proximity to the cluster, the only two that lose the paramagnetic effect (Tyr 19 and Asn 20) belong to the first half of the molecule. This loss of the paramagnetic effect is an important piece of information to conclude that the N-terminal half of the molecule, which also contains two short α-helices in the native state, loses contact completely with the C-terminal part. The same behavior is indicated by the few residual long-range NOEs from the cysteine βCH_2 protons, which all involve residues in the C-terminal half.

Even more striking is the result of the analysis of the backbone dynamics of the *Cv* HiPIP unfolding intermediate. The model-free analysis of the ^{15}N R_1, R_2, and heteronuclear NOE data reinforces the picture of the presence of two distinct motional regimes for the first (up to residue 38) and second (residues 39−85) half of the protein. The average S^2 value in the latter region is nearly twice the value in the first region. Furthermore, approximately one-third of the analyzed residues in the first half of the sequence required values of S^2_f different from 1. As described by Clore et al., this indicates the presence of very fast local motions, characterized by time constants smaller than about 10 ps (*53*). Conversely, for 17 out of the 24 residues in the second half of the sequence amenable to the model-free analysis it was necessary to include into the fittings an exchange contribution to R_2, which is indicative of mobility on the millisecond time scale. The available ^{15}N relaxation data were also used to map the values of the spectral density function at frequencies 0, 60 MHz (=ω_N), and 600 MHz (=ω_H). From the latter analysis it results that the 1−38 portion is characterized by $J(0)$ values smaller than those normally observed for native proteins [the average value is $(1.3 \pm 0.4) \times 10^{-9}$ s, which compares to typical values for native proteins of about $(1.5-2) \times 10^{-9}$ s] and by $J(\omega_H)$ values larger than for native proteins [the average value is $(2.4 \pm 0.5) \times 10^{-11}$ s, against typical values of around 1×10^{-11} s]. These two observations point to extensive backbone fluctuations on the pico- to nanosecond time scale in the first half of the molecule. On the other hand, for the second half of the protein $J(0)$ values are much larger than in native proteins [with an average of $(4.8 \pm 2.3) \times 10^{-9}$ s], and $J(\omega_H)$ values are similar to those of native systems [with an average of $(1.3 \pm 0.6) \times 10^{-11}$ s]. This indicates again that motions on the pico- to nanosecond time scale are less important than in the first half of the molecule and that the second half of the protein is involved in backbone motions on the micro- to millisecond time scale.

Motions in the micro- to millisecond time scale can be directly investigated through off-resonance $R_{1\rho}$ measurements (*40*, *43*, *45*). The results of such measurements are in good agreement with what would be expected from the above discussion. Most of the residues displaying a dependence of the $R_{1\rho}{}^{off,cor}$ on the amplitude of the applied spin-lock that were subjected to the model-free analysis had a R_{ex} contribution to R_2 different from zero. Exceptions from this rule are residues 40, 41, 42, and 58. No off-resonance $R_{1\rho}$ data could be obtained for residue 40. For residue 58 it was observed that the essentially constant $R_{1\rho}{}^{off,cor}$ value was sizably larger than expected for a system of this size in the absence of chemical exchange. This is consistent with the presence of conformational exchange processes with a time constant of the order of 1 μs, which is outside of the experimentally accessible range. In addition, also residue 61, which was not subjected to the model-free analysis due to the lack of reliable NOE data, showed conformational averaging. Overall, the off-resonance $R_{1\rho}$ measurements and the model-free analysis show that none of the residues in the 1−38 region is involved in conformational averaging processes on the micro- to millisecond time scale, whereas 14 to 18 residues (out of the 25 analyzed with either approach in the second half of the molecule) are involved in such motions.

Motions on this time scale are often detected as punctual mobilities and reflect specifically hindered rotations due to steric restraints or isomerizations. Residues in the neighborhood of disulfide bridges also show slow motional properties of this type (*55, 59, 60*). In the present case, the observation of a well-defined hyperfine shift pattern of the βCH_2 cysteine protons rules out any isomerization involving cluster-bound cysteines. Therefore, the slow motions in which several of the residues in the second half of the molecule are engaged must derive from hindered rotations about the backbone dihedral angles caused by the topological restraints imposed by the cysteine coordination to the cluster per se. For example, residues 54−56 are part of a large sequential stretch encompassed by cysteines 46 and 63 and rather far in sequence from either of these two cysteines, and the same holds for residues 68−70. The present data seem to suggest that a complicated sequence of backbone torsion angle changes brings about a "slow" isomerization of the HN vector between different orientations. Overall, this behavior is certainly not consistent with that of a random coil system, which is usually free to rotate about backbone dihedral angles at much higher rates.

Concluding Remarks. A structural model for residues 39−85 of the reduced HiPIP from *Cv* in 4 M GdmCl solution has been proposed after DYANA calculations using 300 constraints of various origin (Table 4). This low number of constraints is the result of disorder, conformational averaging and fast nuclear reorientation rates. The 1−38 part of the protein sequence, which is characterized in the native state by two short helices and by a determined tertiary structure with respect to the cluster, has been found to behave essentially as a random coil polypeptide. Indeed, the chemical shift values are typical of random coil, no long-range NOEs are observed, the $^3J_{HNH\alpha}$ values are averaged to their random coil values, the S^2 order parameter is very small, and $J(\omega_H)$ values are relatively large. The random coil character of the N-terminal half of the intermediate state is consistent with the high solvent exchangeability of the amide protons in this region (*1*). A similar picture holds for the very end of the C-terminal stretch.

Around the coordinated cysteines (43, 46, 63, and 77) there is some structural order imposed by the covalent bonds determined by the metal cluster. However, the RMSD value of the family of 30 conformers for the segment 42−78 is 4.2 Å. This value is only slightly smaller than that obtained without any proton−proton or proton−metal constraints. This means that there is a large degree of conformational freedom within the conformational subspace imposed by the ligation of the four cysteines to the Fe_4S_4 cluster, even in the presence of the various experimental constraints that indicate a nativelike structure in the vicinity of the cluster. This interpretation is supported by the mobility studies, which demonstrate the existence of backbone motions on the milli- to microsecond time scale in the C-terminal half of the partially unfolded protein. On the nano- to picosecond time scale, mobility is here much more restricted than in the random coil segment 1−38. A discrimination of the two long intercysteine loops (47−62 and 64−76) on the basis of the present mobility data is not possible. The relatively low RMSD values in the loop 64−76 (Figure 6) may be due to the higher number of backbone HN T_1^{eff} constraints obtained for this sequential stretch and do not necessarily imply a more restricted mobility.

The unfolding intermediate of *Cv* HiPIP is unique among the hitherto studied unfolded or partially folded proteins as it contains at the same time a highly flexible random coil polypeptide and a more structured part undergoing conformational exchange processes on the milli- to microsecond time scale, where the conformational preferences are not caused by the population of secondary structure elements but imposed by the iron−sulfur cofactor. This underlines the importance of such a cofactor (*11*) as a possible nucleation site of the folding of metalloproteins from a structural point of view.

All the present studies are consistent with the primary role of the Fe_4S_4 cluster in retaining some ordered structure under severe denaturing conditions. Therefore, it may be speculated that the formation of the Fe−S(Cys) bonds is a key step in the folding process when the holoprotein is reconstituted in vitro from iron, sulfide, and the polypeptide (*12*, *61*). This may be a key step also in vivo, although there is not yet experimental evidence. Once the Fe−S(Cys) bonds are established the actual tertiary structure is obtained.

ACKNOWLEDGMENT

We thank Dr. J. A. Cowan, who opened to us the field of HiPIP unfolding and with whom we had many helpful discussions.

SUPPORTING INFORMATION AVAILABLE

Table S1 containing ^1H and ^{15}N NMR resonance assignments of the *Cv* HiPIP unfolding intermediate at 293 K, Table S2 listing ^{15}N NMR relaxation parameters, Table S3 summarizing the results of the model-free analysis, and Table S4 containing the values of the spectral density functions determined from ^{15}N NMR relaxation parameters at 600 MHz proton Larmor frequency. This material is available free of charge via the Internet at http://pubs.acs.org.

REFERENCES

1. Bertini, I., Cowan, J. A., Luchinat, C., Natarajan, K., and Piccioli, M. (1997) *Biochemistry 36*, 9332−9339.
2. Bertini, I., Ciurli, S., and Luchinat, C. (1995) *Struct. Bonding 83*, 1−54.
3. Capozzi, F., Ciurli, S., and Luchinat, C. (1998) *Struct. Bonding 90*, 127−160.
4. Cowan, J. A., and Lui, S. M. (1998) *Adv. Inorg. Chem. 45*, 313−350.
5. Bertini, I., Luchinat, C., Piccioli, M., and Soriano, A. (1998) *Inorg. Chim. Acta 283*, 12−16.
6. Shortle, D. R. (1996) *Curr. Opin. Struct. Biol. 6*, 24−30.
7. Barbar, E., Hare, M., Daragan, V., Barany, G., and Woodward, C. (1998) *Biochemistry 37*, 7822−7833.
8. Dyson, H. J., and Wright, P. E. (1998) *Nat. Struct. Biol. 5*, 499−503.
9. Wong, K. B., Freund, S. M. V., and Fersht, A. R. (1996) *J. Mol. Biol. 259*, 805−818.
10. Buck, M., Schwalbe, H., and Dobson, C. M. (1995) *Biochemistry 34*, 13219−13232.
11. Pascher, T., Chesick, J. P., Winkler, J. R., and Gray, H. B. (1996) *Science 271*, 1558−1560.
12. Bian, S., and Cowan, J. A. (1998) *J. Am. Chem. Soc. 120*, 3532−3533.
13. Winkler, J. R., Wittung, P., Leckner, J., Malmström, B. G., and Gray, H. B. (1997) *Proc. Natl. Acad. Sci. U.S.A. 94*, 4246−4249.
14. Bertini, I., Luchinat, C., and Rosato, A. (1996) *Prog. Biophys. Mol. Biol. 66*, 43−80.
15. Babini, E., Bertini, I., Borsari, M., Capozzi, F., Dikiy, A., Eltis, L. D., and Luchinat, C. (1996) *J. Am. Chem. Soc. 118*, 75−80.
16. Eltis, L. D., Iwagami, S. G., and Smith, M. (1994) *Protein Eng. 7*, 1145−1150.
17. Johnson, R. D., Ramaprasad, S., and La Mar, G. N. (1983) *J. Am. Chem. Soc. 105*, 7205−7206.
18. Banci, L., Bertini, I., Luchinat, C., Piccioli, M., Scozzafava, A., and Turano, P. (1989) *Inorg. Chem. 28*, 4650−4656.
19. Sklenar, V., Piotto, M., Leppik, R., and Saudek, V. (1993) *J. Magn. Reson., Ser. A 102*, 241−245.
20. Vuister, G. W., and Bax, A. (1993) *J. Am. Chem. Soc. 115*, 7772−7777.

21. Wider, G., Macura, S., Kumar, A., Ernst, R. R., and Wüthrich, K. (1984) *J. Magn. Reson. 56*, 207−234.
22. Peng, J. W., and Wagner, G. (1992) *J. Magn. Reson. 98*, 308−332.
23. Kay, L. E., Nicholson, L. K., Delaglio, F., Bax, A., and Torchia, D. A. (1992) *J. Magn. Reson. 97*, 359−375.
24. Kay, L. E., Torchia, D. A., and Bax, A. (1989) *Biochemistry 28*, 8972−8979.
25. Marion, D., and Wüthrich, K. (1983) *Biochem. Biophys. Res. Commun. 113*, 967−974.
26. Barbato, G., Ikura, M., Kay, L. E., Pastor, R. W., and Bax, A. (1992) *Biochemistry 31*, 5269−5278.
27. Eccles, C., Güntert, P., Billeter, M., and Wüthrich, K. (1991) *J. Biomol. NMR 1*, 111−130.
28. Güntert, P., Mumenthaler, C., and Wüthrich, K. (1997) *J. Mol. Biol. 273*, 283−298.
29. Güntert, P., Braun, W., and Wüthrich, K. (1991) *J. Mol. Biol. 217*, 517−530.
30. Wüthrich, K. (1986) in *NMR of Proteins and Nucleic Acids*, Wiley, New York.
31. Bertini, I., and Luchinat, C. (1996) in *NMR of paramagnetic substances*, Coordination Chemistry Review 150, Elsevier, Amsterdam.
32. Banci, L., Bertini, I., Dikiy, A., Kastrau, D. H. W., Luchinat, C., and Sompornpisut, P. (1995) *Biochemistry 34*, 206−219.
33. Bertini, I., Capozzi, F., Luchinat, C., Piccioli, M., and Vila, A. J. (1994) *J. Am. Chem. Soc. 116*, 651−660.
34. Davy, S. L., Osborne, M. J., Breton, J., Moore, G. R., Thomson, A. J., Bertini, I., and Luchinat, C. (1995) *FEBS Lett. 363*, 199−204.
35. Bertini, I., Couture, M. M. J., Donaire, A., Eltis, L. D., Felli, I. C., Luchinat, C., Piccioli, M., and Rosato, A. (1996) *Eur. J. Biochem. 241*, 440−452.
36. Marquardt, D. W. (1963) *J. Soc. Ind. Appl. Math. 11*, 431−441.
37. Press, W. H., Flannery, B. P., Teukolsky, S. A., and Vetterling, W. T. (1988) in *Numerical Recipes in C−The Art of Scientific Computing*, Cambridge University Press, New York.
38. Palmer, A. G., III, Rance, M., and Wright, P. E. (1991) *J. Am. Chem. Soc. 113*, 4371−4380.
39. Peng, J. W., and Wagner, G. (1992) *Biochemistry 31*, 8571−8586.
40. Zinn-Justin, S., Berthault, P., Guenneugues, M., and Desvaux, H. (1997) *J. Biomol. NMR 10*, 363−372.
41. Lipari, G., and Szabo, A. (1982) *J. Am. Chem. Soc. 104*, 4546−4559.
42. Davis, D. G., Perlman, M. E., and London, R. E. (1994) *J. Magn. Reson., Ser. B 104*, 266−275.
43. Desvaux, H., Birlirakis, N., Wary, C., and Berthault, P. (1995) *Mol. Phys. 86*, 1059−1073.
44. James, T. L., Matson, G. B., Kuntz, I. D., and Fisher, R. W. (1977) *J. Magn. Reson. 28*, 417−426.
45. Akke, M., and Palmer, A. G., III (1996) *J. Am. Chem. Soc. 118*, 911−912.
46. Wishart, D. S., Bigam, C. G., Holm, A., Hodges, R. S., and Sykes, B. D. (1995) *J. Biomol. NMR 5*, 67−81.
47. Schwalbe, H., Fiebig, K. M., Buck, M., Jones, J. A., Grimshaw, S. B., Spencer, A., Glaser, S. J., Smith, L. J., and Dobson, C. M. (1997) *Biochemistry 36*, 8977−8991.
48. Bertini, I., Donaire, A., Feinberg, B. A., Luchinat, C., Piccioli, M., and Yuan, H. (1995) *Eur. J. Biochem. 232*, 192−205.
49. Wang, P. L., Donaire, A., Zhou, Z. H., Adams, M. W. W., and La Mar, G. N. (1996) *Biochemistry 35*, 11319−11328.
50. Aono, S., Bentrop, D., Bertini, I., Donaire, A., Luchinat, C., Niikura, Y., and Rosato, A. (1998) *Biochemistry 37*, 9812−9826.
51. Abragam, A. (1961) in *The Principles of Nuclear Magnetism*, Oxford University Press, Oxford, England.
52. Mandel, M. A., Akke, M., and Palmer, A. G., III (1995) *J. Mol. Biol. 246*, 144−163.
53. Clore, G. M., Szabo, A., Bax, A., Kay, L. E., Driscoll, P. C., and Gronenborn, A. M. (1990) *J. Am. Chem. Soc. 112*, 4989−4991.
54. Farrow, N. A., Zhang, O., Forman-Kay, J. D., and Kay, L. E. (1995) *Biochemistry 34*, 868−878.
55. Buck, M., Schwalbe, H., and Dobson, C. M. (1996) *J. Mol. Biol. 257*, 669−683.
56. Peng, J. W., and Wagner, G. (1995) *Biochemistry 34*, 16733−16752.
57. Deverell, C., Morgan, R. E., and Strange, J. H. (1970) *Mol. Phys. 18*, 553−559.
58. Wennerström, H. (1972) *Mol. Phys. 1*, 69−80.
59. Redfield, C., Smith, R. A. G., and Dobson, C. M. (1994) *Nat. Struct. Biol. 1*, 23−29.
60. Szyperski, T., Luginbuhl, P., Otting, G., Güntert, P., and Wüthrich, K. (1993) *J. Biomol. NMR 3*, 151−164.
61. Natarajan, K., and Cowan, J. A. (1997) *J. Am. Chem. Soc. 119*, 4082−4083.
62. Carter, C. W. J., Kraut, J., Freer, S. T., Xuong, N.-H., Alden, R. A., and Bartsch, R. G. (1974) *J. Biol. Chem. 249*, 4212−4215.
63. Koradi, R., Billeter, M., and Wüthrich, K. (1996) *J. Mol. Graphics 14*, 51−55.

BI982647Q